Influence of Land Cover and Soil Moisture on the Horizontal Distribution of Sensible and Latent Heat Fluxes in Southeast Kansas during IHOP_2002 and CASES-97

MARGARET A. LEMONE, FEI CHEN, JOSEPH G. ALFIERI,* AND MUKUL TEWARI
National Center for Atmospheric Research,+ Boulder, Colorado

BART GEERTS AND QUN MIAO
Department of Atmospheric Sciences, University of Wyoming, Laramie, Wyoming

ROBERT L. GROSSMAN
Colorado Research Associates, Boulder, Colorado

RICHARD L. COULTER
Argonne National Laboratory, Chicago, Illinois

(Manuscript received 18 August 2005, in final form 9 June 2006)

ABSTRACT

Analyses of daytime fair-weather aircraft and surface-flux tower data from the May–June 2002 International H_2O Project (IHOP_2002) and the April–May 1997 Cooperative Atmosphere Surface Exchange Study (CASES-97) are used to document the role of vegetation, soil moisture, and terrain in determining the horizontal variability of latent heat LE and sensible heat H along a 46-km flight track in southeast Kansas. Combining the two field experiments clearly reveals the strong influence of vegetation cover, with H maxima over sparse/dormant vegetation, and H minima over green vegetation; and, to a lesser extent, LE maxima over green vegetation, and LE minima over sparse/dormant vegetation. If the small number of cases is producing the correct trend, other effects of vegetation and the impact of soil moisture emerge through examining the slope $\Delta_{xy}\text{LE}/\Delta_{xy}H$ for the best-fit straight line for plots of time-averaged LE as a function of time-averaged H over the area. Based on the surface energy balance, $H + \text{LE} = R_{\text{net}} - G_{\text{sfc}}$, where R_{net} is the net radiation and G_{sfc} is the flux into the soil; $R_{\text{net}} - G_{\text{sfc}} \sim$ constant over the area implies an approximately -1 slope. Right after rainfall, H and LE vary too little horizontally to define a slope. After sufficient drying to produce enough horizontal variation to define a slope, a steep (~ -2) slope emerges. The slope becomes shallower and better defined with time as H and LE horizontal variability increases. Similarly, the slope becomes more negative with moister soils. In addition, the slope can change with time of day due to phase differences in H and LE. These trends are based on land surface model (LSM) runs and observations collected under nearly clear skies; the vegetation is unstressed for the days examined. LSM runs suggest terrain may also play a role, but observational support is weak.

1. Introduction

This paper explores the relationship of surface heterogeneity to low-level fluxes of sensible heat and latent heat, using aircraft and surface-based data collected in May–June 2002 in southeast Kansas as part of the International H_2O Project (IHOP_2002; Weckwerth et al. 2004), and data collected in April–May 1997 as part of the Cooperative Surface Atmosphere Exchange Study (CASES-97; LeMone et al. 2000). This study is possible because aircraft data were collected along the same flight track in both experiments. The track (the "eastern track" in Fig. 1; also see Fig. 2) is characterized by a mix of mostly grassland and winter wheat, with trees bordering many fields and waterways. The track extends across the eastern side of the Walnut River watershed and into the watershed to the east. While the vegetation types were similar for both field experiments, the phase in their seasonal cycles was

* Current affiliation: Purdue University, West Lafayette, Indiana.

+ The National Center for Atmospheric Research is sponsored by the National Science Foundation.

Corresponding author address: Margaret A. LeMone, NCAR Foothills Laboratory, 3450 Mitchell Lane, Boulder, CO 80301.
E-mail: lemone@ucar.edu

DOI: 10.1175/JHM554.1

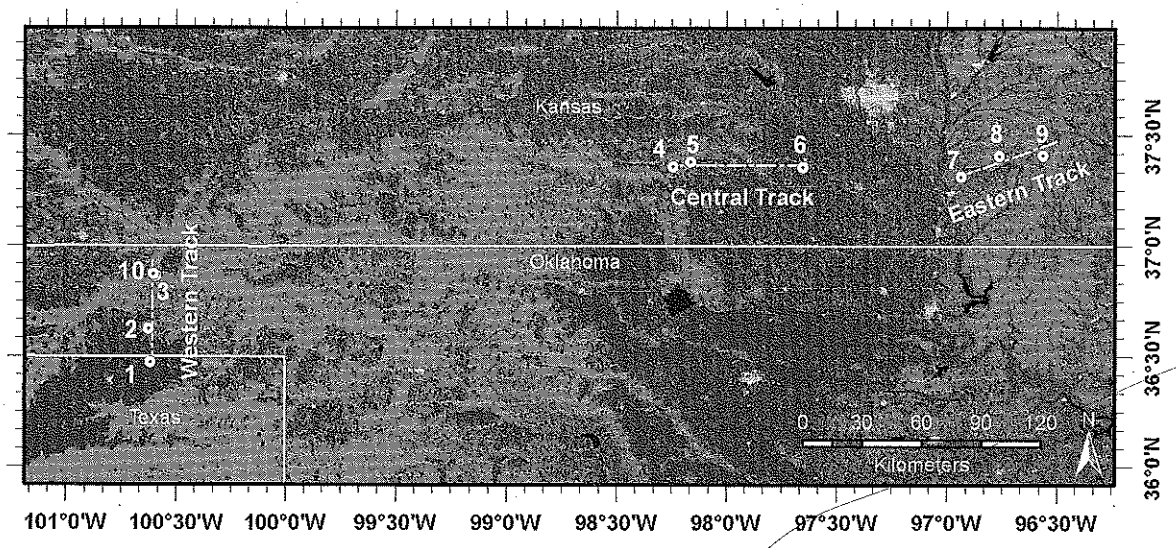

FIG. 1. Location of the three IHOP_2002 BLH flight tracks, superimposed on land use. The western track and central track are 60 km in length, with the eastern track 45.6 km. Light gray is grasslands, darker gray is mainly winter wheat, and black areas are water. Numbers correspond to surface-flux stations.

quite different. This contrast allows the results to emerge with a clarity not possible otherwise.

Since the 1980s, Anthes (1984), Segal et al. (1988), Pielke et al. (1991), Chen et al. (2001), and others have used numerical simulations to document the importance of land surface characteristics to local weather and climate. Chen et al. (2001) demonstrated that replacing the older "bucket" soil-moisture model with the Oregon State University (OSU) Land Surface Model (LSM; Pan and Mahrt 1987; Chen et al. 1996) improved 24–48-h precipitation forecasts in the Eta Model, as much as doubling the horizontal resolution. Trier et al. (2004) provide two specific examples of surface processes reinforcing convective initiation in the southern Great Plains: in one case the air is destabilized through enhanced PBL growth over warmer surfaces and in the second forcing and destabilization results from 100-km-scale circulations generated by differential surface heating.

The goal of IHOP_2002 is to improve prediction of convective precipitation in numerical weather prediction models by improving the collection and use of water vapor data, and improving representation of the evolution of water vapor. Surface processes are emphasized because of their importance in the initiation and evolution of precipitating convection. This paper focuses on the relationship of surface characteristics (land cover, soil moisture, soil type, elevation) to surface fluxes on fair-weather days. The data and results discussed herein will be used to evaluate and improve the Noah land surface model (Ek et al. 2003) and the performance of the Weather Research and Forecasting (WRF) model in representing fair-weather boundary layer evolution. The impact of these improvements will be tested through evaluations of IHOP_2002 convective-initiation simulations.

This paper demonstrates that land cover has a significant impact on the horizontal distribution of near-surface sensible heat flux H and latent heat flux LE along the eastern track during IHOP_2002 and CASES-97, but soil moisture appears to influence the relative magnitude of their horizontal variability. The data collection and analysis strategy are discussed in section 2. Section 3 presents the horizontal flux distribution and relates it to surface properties. Section 4 looks at horizontal flux variability in more detail, and uses observed data and LSM results to investigate the conditions driving the horizontal flux variability (rainfall, land cover, soil type, terrain). The results are discussed and summarized in section 5.

2. Data collection and data analysis

a. Aircraft data: Fluxes, surface characteristics, and boundary layer depth

Aircraft data for both field experiments were collected using the University of Wyoming King Air gust-probe aircraft. For CASES-97, aircraft-relative winds were measured by a Rosemount 858AJ/1332 differential pressure gust-probe system. Aircraft position and motion relative to the ground were measured by a Honeywell Laseref SM inertial navigation system. Aircraft altitude was based on a King KRA5 radar altimeter for heights below 610 m and an APN159 radar altimeter for

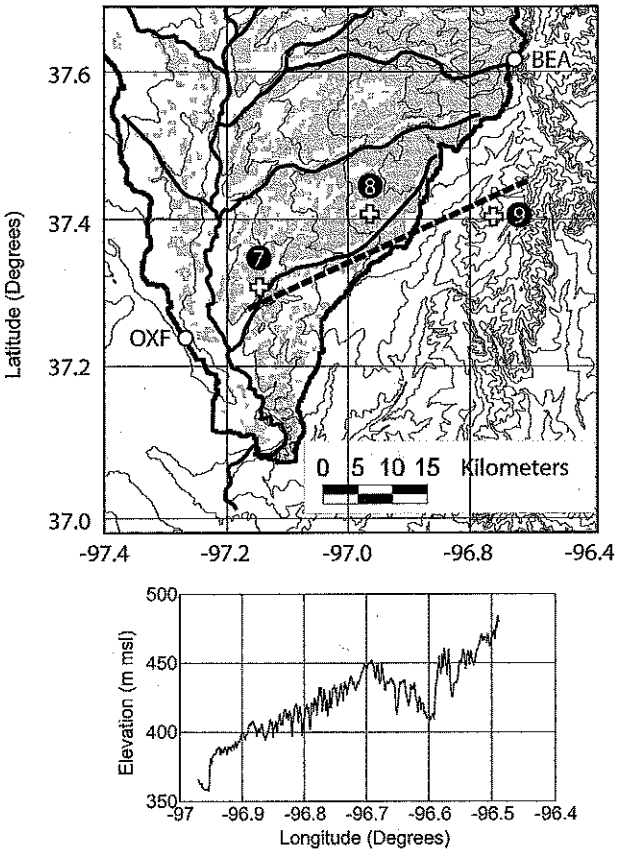

FIG. 2. (top) Plan view of IHOP_2002 observations superimposed on contours (interval = 20 m); shading in the Walnut River watershed (outlined) = grassland; (bottom) elevation beneath the eastern track (based on pressure altitude minus radar altitude along flight leg at ~65 m). OXF = radar wind profiler at Oxford, KS (37.27°N, 97.19°W); BEA = radar wind profiler at Beaumont, KS (37.63°N, 96.54°W). Numbers and + symbols correspond to surface-flux stations; dashed line = eastern track.

heights above 610 m. The mixing ratio Q was measured using the LiCor 6262 gas analyzer, the radiometric surface temperature T_s was measured with a PRT-5 radiometer, and potential temperature Θ was calculated from the pressure from a Rosemount 1201 sensor and air temperature measured as described in Friehe and Khelif (1992). Data were recorded at 50 Hz.

The King Air instrument package and software were slightly different for IHOP_2002. The normalized differential vegetation index (NDVI) was estimated from an Exotech radiometer, using the relationship

$$\mathrm{NDVI} = \frac{r_4 - r_3}{r_4 + r_3}, \tag{1}$$

where r_4 is the amount of electromagnetic radiation reflected in the near-infrared at 0.762–0.898 μm, and r_3 is the amount of electromagnetic radiation reflected in the red at 0.629–0.687 μm. The aircraft location was corrected using GPS to within 100 m horizontally (A. Rodi 2006, personal communication), so that T_s, NDVI, and aircraft video images could easily be correlated with surface features. A reverse flow thermometer measured air temperature, and a Heiman KT-19.85 radiometer sensed T_s. Data were recorded at 25 Hz.

Figure 1 shows the three tracks used for IHOP_2002 Boundary Layer Heterogeneity (BLH) missions, which were designed to document the effects of the surface on BL thermodynamic fluxes and structure. The flight-track locations extended from the Oklahoma Panhandle to southeastern Kansas, to sample a large range of precipitation, soils, and land-cover types. This paper focuses on the eastern track, shown in Fig. 2; fluxes on the western track are documented by Kang et al. (2007). From Table 1, the eastern track has greener and denser vegetation (higher NDVI), cooler T_s, and higher rainfall than the western track. The central track has intermediate characteristics.

Each King Air mission consisted of multiple straight-and-level legs along a single track, interspersed with soundings to check convective boundary layer depth (Table 2). In the IHOP_2002 BLH missions, some legs were always flown at ~70 m above ground level (AGL), with at least one other height within the boundary layer (BL) represented. The flight pattern changed with the research emphasis, with more 70-m legs for flux missions, and legs divided more evenly between two and four heights for BL structure missions. For typical CASES-97 missions, four sets of legs at four levels within the BL were flown along the IHOP_2002 eastern track, with the lowest level at 30–40 m AGL. The lowest legs (below 100–150 m) were flown at a roughly constant height above the ground, while the higher legs were flown according to pressure altitude, so that altitude above the ground varied around the specified leg height.

"Total" grand-average IHOP_2002 and CASES-97 fluxes along the eastern track for a given day were calculated in a multiple-step procedure following LeMone et al. (2003). First, time series for Θ, Q, and vertical velocity W for each leg were detrended by subtracting out the best-fit line based on linear regression. Second, the mixing ratio was shifted 0.30 s earlier and the temperature 0.1 s earlier to correct for instrument time lag and the physical separation of the thermodynamic sensors from the vertical-velocity sensors on the aircraft.[1]

[1] For IHOP_2002, the lag time for mixing ratio was 0.32 s, the result of a coarser data resolution and a compromise between the 0.3 s used for CASES-97 data analysis and the 0.35 based on looking at the relationship between vertical velocity and mixing ratio at 70 m.

TABLE 1. Characteristics of the western and eastern IHOP_2002 flight tracks.

(a) Surface conditions along the flight track on King Air BLH mission days

West	Avg time (UTC)	NDVI	T_s (°C)	East	Avg time (UTC)	NDVI	T_s (°C)
19 May	18.075	0.134	37.0	27 May	17.429	0.641	27.6
20 May	17.925	0.137	37.5	30 May	18.063	0.561	36.0
25 May	18.619	0.147	42.3	17 Jun	18.742	0.633	32.1
29 May	19.087	0.161	39.5	20 Jun	18.738	0.647	35.6
7 Jun	18.181	0.200	—	22 Jun	19.059	0.631	35.6

(b) Rainfall (mm) at surface stations along the track

West	Station 1	2	3	10	East	Station 7	8	9
	154	69	72	62		175	296	250

Third, the resulting time series [$\theta(t)$, $q(t)$, and $w(t)$] were multiplied to form $\theta(t)w(t)$ and $q(t)w(t)$ time series. Fourth, these products were averaged into increments (0.01° longitude for CASES-97, 1 km for IHOP_2002) and converted to H and LE. For each leg, this procedure resulted in a set of 0.97- or 1-km segments whose fluxes, when averaged, are close to the leg-average fluxes. Fifth, data for each leg were smoothed using a 4-km running-mean average. Finally, the smoothed fluxes at corresponding points were averaged to form the grand-average leg. For IHOP_2002, the 1-km data for each leg were interpolated to common geographical points before averaging in time. While the interpolation has the effect of smoothing the 1-km data slightly, this should not significantly alter fluxes after smoothing with running means 4 km and longer to obtain statistical robustness.

For comparison, we calculated "high frequency" fluxes for the IHOP_2002 days using a procedure similar to that for the total fluxes except that the 1-km average fluxes for each leg were calculated using fluctuations relative to the corresponding 1-km mean.

We focus on the total fluxes because their magnitudes should be similar to measured and modeled surface fluxes. In the First International Satellite Land Surface Climatology Project (ISLSCP) Field Experiment (FIFE), high-pass filtering the data to remove fluctuations of wavelength >5 km resulted in underestimates in both H and LE (Grossman 1992; Kelly et al. 1992); in a more complete analysis, Lenschow et al. (1994) obtain a similar result. For the IHOP_2002 cases examined (Table 3), the leg-averaged high-frequency fluxes were between 77% and 88% of the leg-averaged total fluxes. The disadvantage is that the total fluxes include "mesoscale" motions, whose larger scales lead to more random error, and which may lead to a longer "memory" of the upstream surface. Further, linear-trend removal is not optimum when the time series include an abrupt change.

Table 4 shows estimates of the fractional random error $\sigma^*(F)$ for average total H and LE for each day. We calculated $\sigma^*(F)$ for each leg following Mann and Lenschow (1994) via

$$\sigma^*(F)_L = \left(\frac{2\lambda_F}{L}\right)^{1/2}\left(\frac{1 + r_{w,s}^2}{r_{w,s}^2}\right)^{1/2}, \qquad (2)$$

TABLE 2. Boundary layer King Air flights and environmental conditions along eastern track for CASES-97 (C) and IHOP_2002 (I); z_i = boundary layer depth. Numbers in parentheses refer to equations in the text.

Date	65-m legs	Other heights	Days after rainfall	65-m wind (m s^{-1})	z_i center time (m)	$-L$ (4) (m)	L_{co} (3) (km)	Clouds
29 Apr 97C	4[b]	12	>7	S 10[a]	850	100	3.6	Broken Ci
10 May 97C	4[b]	12	2	SSW 5–6[a]	1200	26	2.5	Clear
27 May 02I	8	7	0	161°/5.5	—	98[c]	—	Ci, CiSt, AltoCu, small Cu later
30 May 02I	8	8	3/5.5[d]	159°/3.9	900	21[c]	1.8	Ci; small Cu; haze at BL top
17 Jun 02I	6	12	1.7	201°/7.7	1240	115[c]	4.4	Cu hu streets
20 Jun 02I	5	9	4.7	162°/5.3	1250	46[c]	3.3	Scat Cu hu and Ci
22 Jun 02I	10	9	6.7	179°/9.4	1260	218[c]	5.8	Cu hu streets

[a] Wind estimate from aircraft and profilers combined; from Table 1 of LeMone et al. (2003).
[b] 30–40 m AGL.
[c] D. Strassberg (2005, personal communication).
[d] Three days after light (5–10 mm) rain on 27 Jun; 5.5 days after heavy rain.

TABLE 3. Comparisons of fluxes averaged from grand-average legs. Primes indicate "high frequency" fluxes computed with respect to 1-km block averages; unprimed fluxes are "total" fluxes, computed with respect to flight-leg linear trends.

Date	H	LE	H'	LE′	H'/H	LE′/LE
30 May	91.606	439.77	81.05	338.19	0.88	0.77
17 Jun	92.78	382.01	73.3	333.12	0.79	0.87
20 Jun	69.1	421.31	59.07	356.47	0.85	0.85
22 Jun	92.55	416.68	78.25	363.79	0.85	0.87

TABLE 4. Fractional random uncertainty σ^* in H and LE averaged over all the low-level legs, based on Mann and Lenschow (1994) and Lenschow (1995).

Date	Low legs	Average H (W m^{-2})	σ^*_H	Average LE (W m^{-2})	σ^*_{LE}
29 Apr 1997	4	119	0.06	162	0.09
10 May 1997	4	102	0.11	232	0.08
30 May 2002	8	94	0.063	380	0.103
17 Jun 2002	6	95	0.086	381	0.106
20 Jun 2002	5	68	0.093	420	0.107
22 Jun 2002	10	92	0.063	423	0.080

and then combined the results for all N legs as described in LeMone et al. (2003). In (2), s is a scalar, L is the length of the flight leg (~46 km), λ_F is the integral scale for ws, found from the ws − spectrum as described in Lenschow (1995), and $r_{w,s}$ is the correlation between w and s. Relative to the values in the table, $\sigma^*(F)$ increases by a factor of $\sim(46/4)^{1/2} = 3.39$ for 4-km averages along the grand-average leg. The IHOP_2002 random errors are comparable to those for CASES-97 in spite of more flight legs because changing the height of the lowest flight legs from 35 to 70 m leads to roughly a doubling of λ_F and thus a need for twice as many legs to get the same random error.

b. Surface-station data: Fluxes

Flux stations along the eastern track were all grassland sites, located at positions 7, 8, and 9 in Figs. 1 and 2. Half-hour averages of the terms in the surface energy budget (H and LE from eddy correlation, soil heat flux G_{sfc}, and net radiation R_{net}) from these sites are available at http://www.rap.ucar.edu/research/land/observations.php, along with meteorological variables (temperature and mixing ratio at 2 m, wind at 10 m, precipitation) and soil moisture at 5 cm. Also collected were 5- or 15-min profiles of several soil characteristics including soil moisture and temperature, at six depths to 0.6–0.9 m. The automatically recorded data were supplemented at 7–10-day intervals with photographs and manual observations of soil moisture and various vegetation characteristics. Because of instrument malfunction, the IHOP_2002 LE values used here were estimated as a residual from the surface energy budget. For the two CASES-97 case study days used here, LeMone et al. (2002) found that the fluxes were slightly underestimated, such that H + LE ~ 0.9–0.94 (R_{net} − G_{sfc}). For IHOP_2002, LE was available after ~12 June at station 9; the resulting residual was ~0.1(R_{net} − G_{sfc}) but changed sign from day to day.

Because H was calculated from sonic temperatures using LE (Schotanus et al. 1983), the H measurements used here are too low by up to ~10%–20% on days when the fast-humidity instrument malfunctioned (produced obviously too low LE). This estimate is based on iteratively correcting H using LE based on surface energy balance.

c. Comparison of aircraft and surface-station fluxes

For IHOP_2002, surface H values extrapolated downward from linearly regressed aircraft leg-average total H profiles are about 10% lower than fluxes based on tower measurements, with total leg-average LE values within 5% except for 30 May, when the values differed by ~15%. Agreement is slightly better with corrected H. However, the H average for stations 7–9 is probably too low and the LE average too high, compared to the actual surface average, since all three sites are on grassland and the main other type of land cover (dormant winter wheat) should have higher H and lower LE than the green grasses. During CASES-97, King Air LE was similar to surface values given the large scatter, but H was up to 30% lower than the surface fluxes (LeMone et al. 2002).

d. Supplementary boundary layer depth estimates

The Argonne National Laboratory's Atmospheric Boundary Layer Experiments (ABLE) facility radar wind profilers at Beaumont and Oxford, Kansas, were used to obtain boundary layer depth near the ends of the eastern track (Fig. 2). The vertical resolution is of the order of 60 m at Beaumont and 100 m at Oxford for CASES-97, and 60 m for both for IHOP_2002. Boundary layer height is defined as center height of the gate just below the maximum signal-to-noise ratio (SNR) drop-off rate with height (Coulter and Holdridge 1998).

The Wyoming Cloud Radar (WCR) was used to determined PBL depth along the flight track. The WCR is a 3-mm (95 GHz) multiantenna Doppler radar (Pazmany et al. 1994). During IHOP_2002, the radar's two antennas looked vertically up and down from the aircraft; the along-beam data are resampled in 15-m gates after applying a spline fit to 4-m samples. The along-beam (vertical) resolution is O(30 m), and the nearest

reliable gates are centered 120 m below and 105 m above the aircraft, resulting in a 225-m "blind" zone approximately centered on the aircraft. Echo strength is measured in terms of equivalent reflectivity, which is derived from power under the assumption that the scatterers are spherical water droplets.

The WCR BL depth z_{i_WCR} is determined from the equivalent reflectivity above plumes (Miao et al. 2006) after vertical (three gates or 45 m) and horizontal (10 s or ~830 m) smoothing. Usually, z_{i_WCR} is found from the upward-looking beam, and defined as where the range-corrected reflectivity reaches a minimum—between the drop-off at plume top and the increase in reflectivity due to range-corrected noise. For the downward-looking beam, z_{i_WCR} is taken as the height of an arbitrary reflectivity value ranging between −28 and −26 dBZ. This level is characterized by a large reflectivity gradient. Since the scatterers are small insects trying to fly downward, reflectivity becomes small between plumes and BL depth is often not detectable there (Geerts and Miao 2005).

3. Results

a. Environmental conditions

With the exception of 27 May (IHOP_2002) when light rain fell, the days examined (Table 2) had clear skies to scattered clouds, and wind from ~SSW–SE, with speeds ranging from slightly less than 4 m s^{-1} on 30 May 2002 to 10 m s^{-1} on 29 April 1997. From Fig. 3, the rain and associated cloudiness significantly altered the surface energy budget on 27 May. Since our focus is on the effects of surface heterogeneity, 27 May will not be included in the analysis. The curves for net radiation (R_{net}), H, LE, and heat flux into the soil (G_{sfc}), are relatively smooth on the remaining six days, consistent with the lack of significant cloudiness (Fig. 3; Fig. 3 of LeMone et al. 2002; Fig. 9 of LeMone et al. 2000). The June days represent a single dry-down event (Table 2).

The land-use maps (Figs. 1, 2) show a higher density of crops (mainly winter wheat) to the west and mainly grasslands to the east, relative to the eastern track and for at least 100 km to the south. The band of winter wheat extends south to the Oklahoma–Kansas border; south of the border, the winter wheat band extends southwestward to beyond the Oklahoma–Texas border. Aircraft videos and surface site visits show land use along the flight track to be similar for CASES-97 and IHOP_2002. The dominant soil type along the flight track is silty clay loam (State Soil Geographic Database). Rainfall was ample (Table 1; Yates et al. 2001) and frequent (Chen et al. 2003, 2007) for both field programs, so the vegetation was not stressed.

b. Horizontal variability in low-level fluxes along the flight track

The H patterns, in Fig. 4 for IHOP_2002 and Fig. 5 for CASES-97, have consistent behavior for both experiments. For the IHOP_2002 days, there are H maxima around −96.9° (**A**) and −96.7° (**A′**), separated by a minimum from −96.77° to −96.8°. The pattern is reversed for CASES-97, with a well-defined H minimum around **A** on 29 April 1997 and a broader H minimum on 10 May 1997 spanning the same location; and secondary H minima around **A′** on 10 May, and slightly west of **A′** on 29 April. At the east end of the track, H increases eastward on three of the four IHOP_2002 days, and decreases eastward on the two CASES-97 days.

The LE patterns in Figs. 4 and 5 are not as well defined as the H patterns, with horizontal fluctuations sometimes less than the temporal standard deviations. Such behavior has also been noted by Mahrt (2000). However, there are LE minima around **A′** for all the IHOP_2002 days except 22 June, corresponding to the IHOP_2002 H maxima. On 22 June, the LE minimum at **A** corresponds to the major H maximum, and the LE maximum corresponds to the H minimum east of **A′**. Also, the CASES-97 data show LE maxima near **A** that correspond roughly with the westernmost CASES-97 H minima and IHOP_2002 H maxima.

Except for the expected smaller values, amplitudes, and standard deviations, the IHOP_2002 fluxes relative to 1-km averages in Fig. 6 resemble those in Fig. 4 closely. The similarity of the flux trends near the leg ends suggests that linear trend removal to produce the fluxes in Figs. 4 and 5 did not have a significant effect.

Comparing Figs. 4–6 to Fig. 7, the major features in the flux patterns are correlated with T_s, NDVI, and land-use patterns along the flight track. The T_s maxima and NDVI minima for IHOP_2002 correspond to areas of senescent-to-harvested (~15 June) winter wheat, with the broadest extrema at **A** and **A′**, and more localized extrema at the riparian zone **B**. Locations **A** and **A′** tend to have high H values and, to a lesser degree, low LE values. The low-T_s, high-NDVI areas correspond to green grass, low H, and to a lesser degree, high LE. In CASES-97, the patterns reverse, with low H, high LE, low T_s, and high NDVI over the winter wheat, which grows rapidly in late April through middle May; and high H, low LE, high T_s, and low NDVI over the grasslands, which are largely dormant on 29 April, and starting to green up by 10 May. The association of H and LE with T_s is discussed in more detail for CASES-97 in Grossman et al. (2005). The small horizontal T_s variability on 17 June 2002 relates to rain on 15–16 June (Table 2).

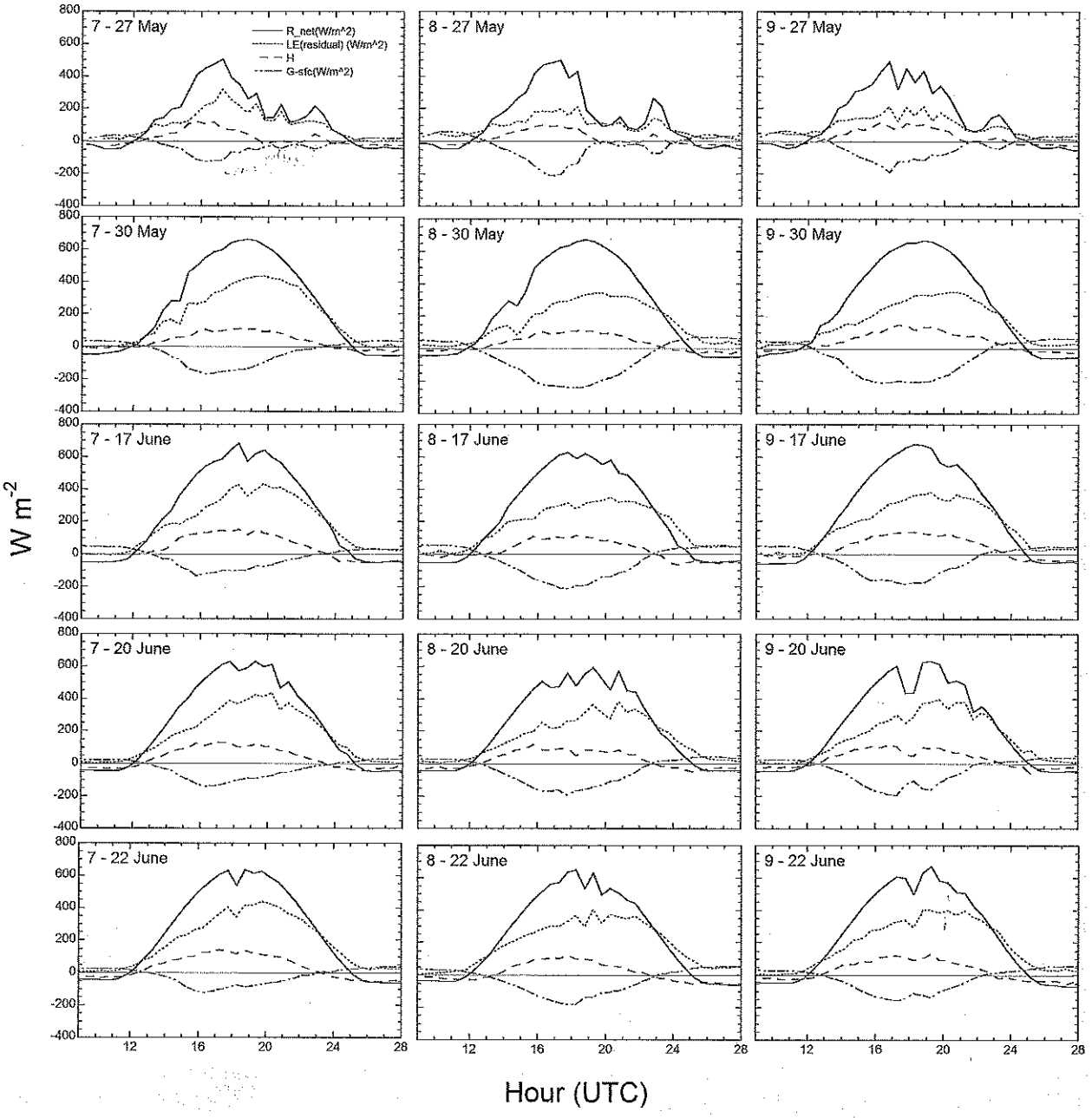

FIG. 3. For the five IHOP_2002 days of Table 2, terms in energy budget $R_{net} = H + LE + G_{sfc}$ at stations 7, 8, and 9. Lines: R_{net}: solid; H: dash; $-G_{sfc}$: dot–dash; LE: dotted. Note that LE is found as a residual assuming an energy balance. Solar noon is around 1830 UTC. All stations are located on grassland.

Table 5 lists the grand-average 4-km filtered flux-T_s, flux–NDVI, and T_s–NDVI correlations along the flight track, and shows that H is slightly more strongly related to NDVI than to T_s, while LE relationships to both are weaker. Not surprisingly, the largest correlations are for 22 June, which combined the smallest random error (Table 4) with the largest horizontal variability (Figs. 4, 6). For the three June days, the correlation of T_s with NDVI increases with time after rainfall (Table 2).

Some of the day-to-day differences between the flux distributions appear to be related to the range of land surface heterogeneity scales felt at flight level. We use two qualitative criteria, the scale length L_{co} and the stability as expressed by the Obukhov length $-L$ (Table 2). The scale L_{co} (Raupach and Finnigan 1995), listed in Table 2, can be used as a crude measure of the minimum length scale that can affect flux distribution. It is based on the time scale for air

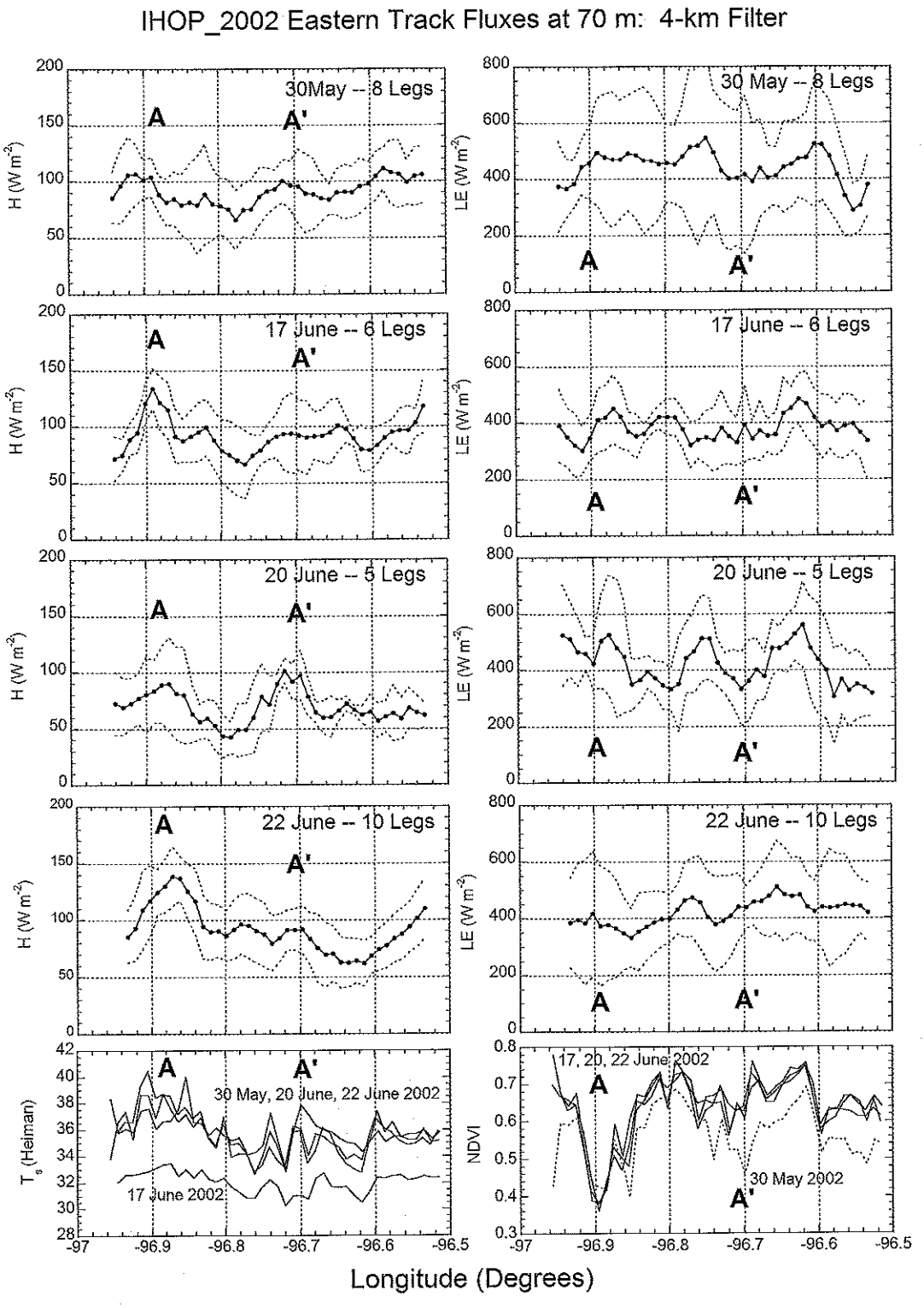

FIG. 4. For the four IHOP_2002 case study days. (top four rows) Four-kilometer running-mean "total" grand-average fluxes ($\overline{F}$) of sensible heat (H) and latent heat (LE). Dotted lines show $\overline{F} \pm \sigma$, where $\sigma^2 = (1/N)\Sigma_{i=1}^{N}(F_i - \overline{F})^2$, with F_i = 4-km-averaged flux along the ith leg and N = number of legs. (bottom row) The grand-average ~1 km NDVI and T_s. **A** and **A'** correspond to areas of winter wheat along and to the south of the flight track.

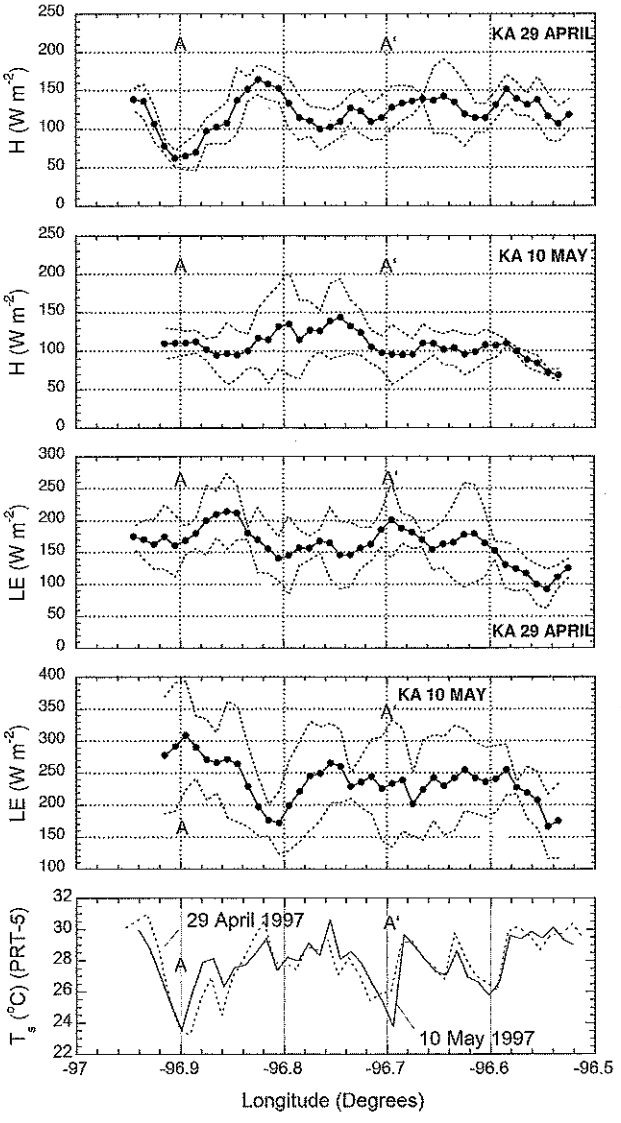

FIG. 5. Same as in Fig. 4, but for CASES-97, except that leg-mean flux time trend taken out before computing σ, since the flight legs were flown in the morning (1500–1830 UTC 29 April; 1530–1830 UTC 10 May). (bottom row) One-kilometer grand-average leg T_s. (top four rows) Adapted from LeMone et al. (2003).

from the surface to reach the top of the boundary layer, given by

$$L_{co} = C_{co}\frac{Uz_i}{w_*}, \tag{3}$$

where U is the boundary layer wind speed, z_i is the boundary layer depth, C_{co} ~0.8 (Mahrt 2000), and w_* is the convective velocity scale, $w_* = [gz_i(\overline{w\theta}_{v,sfc}/\Theta_{v,sfc})]^{1/3}$, where g is the acceleration of gravity, $\overline{w\theta}_{v,sfc}$ is the surface virtual temperature flux, and $\Theta_{v,sfc}$ is the virtual potential temperature at the surface. The Obukhov length L is given by

$$L = -\frac{\Theta_{v,sfc}u_*^3}{kg\overline{w\theta}_{v,sfc}}, \tag{4}$$

where u_* is the friction velocity and k is the von Kármán constant (here 0.4). In (3) and (4), we use values roughly applicable to the center time of the flight pattern (average for CASES-97, interpolated values for IHOP_2002). We include L since the effective flux footprint decreases in size and its peak becomes closer to the measurement site as the boundary layer becomes more convective (e.g., Schuepp et al. 1992).

The results, in Table 2, are consistent with the impact of smaller scales on the fluxes at flight level being reduced on days with strong wind and weak buoyancy flux. For IHOP_2002 and CASES-97, the westernmost H extremum at **A** is most prominent horizontally for 29 April 1997 and 17 and 22 June 2002, which have large L_{co} and $-L$. From Fig. 7, these differences are consistent with the winter wheat area being broader upstream (south) of **A** than upstream of **A′**. Conversely, the H extrema at **A** and **A′** are comparable on 30 May 2002, 20 June 2002, and 10 May 1997, days with smaller L_{co} and $-L$, suggesting the fetch at **A′** is large enough that the differences in fetch do not matter. For LE, the extremum at **A** dominates on 22 June 2002 and to a lesser degree on 29 April 1997. Both have large L_{co} and $-L$ but perhaps more significantly also have the best statistical sample (Table 4). Note that the ~2 km wide riparian zone at **B** does not have a clear impact on H or LE on any of the days observed.

4. Effects of rainfall—The slope Δ_{xy}LE/$\Delta_{xy}H$

a. Definition of $\Delta_{xy}LE/\Delta_{xy}H$ and how it is estimated

In the foregoing, areas of high H often correspond to areas of low LE, and vice versa. To evaluate horizontal variability in IHOP_2002 and CASES-97 from a different perspective, we examine the slope of the best-fit straight line in plots of LE as a function of H, averaged over a given time interval, as illustrated for 29 April 1997 in Fig. 8. In the figure, H and LE varied by roughly 250 W m^{-2}, from high-H and low-LE values over bare ground to low-H and high-LE values over green vegetation, producing a slope $\Delta_{xy}LE/\Delta_{xy}H = -0.92$.

The association of higher LE values with lower H values (compared to the horizontal average) and vice versa, and the resulting negative $\Delta_{xy}LE/\Delta_{xy}H$ slopes follow from the surface energy balance:

$$R_{net} - G_{sfc} = H + LE, \tag{5}$$

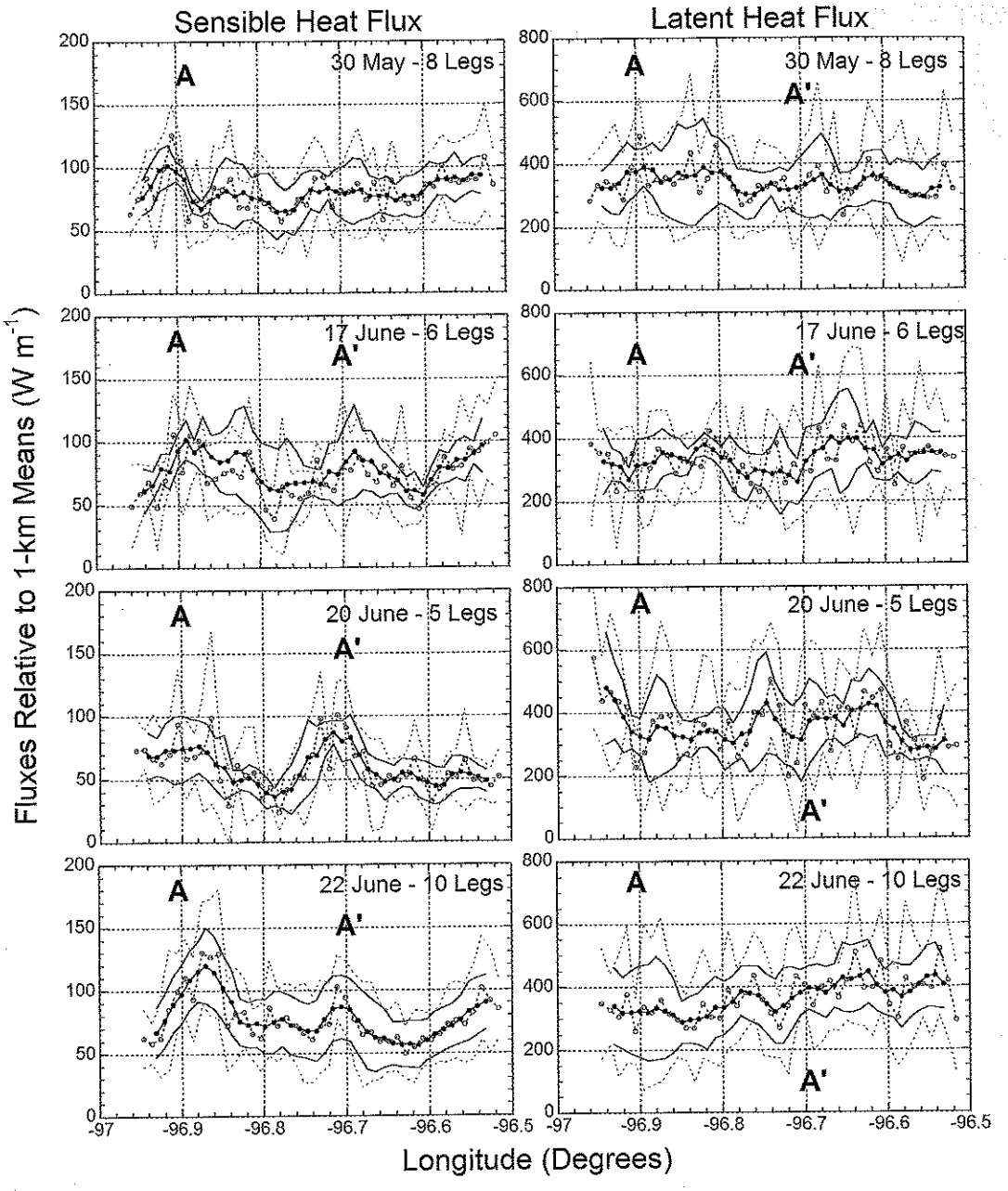

FIG. 6. Same as in Fig. 4, but for fluxes relative to 1-km averages (solid lines and circles). Also, grand-average 1-km interpolated fluxes appear along with their standard deviations (dashed lines, open circles).

as long as horizontal changes in H and LE are large compared to horizontal changes in $R_{net} - G_{sfc}$. Here $R_{net} - G_{sfc}$ = constant, H + LE = constant, and Δ_{xy}LE/$\Delta_{xy}H = -1$.

Based on CASES-97 data, LeMone et al. (2003) suggested that the available energy H + LE ~ constant with clear skies and several days after the last rainfall. Clouds create a more complex net radiation field (Fig. 3), and the fluxes tend to be more uniform right after rainfall (Mahrt 2000; Yates et al. 2001; LeMone et al. 2003). To define the slope using surface-flux stations, a variety of land uses must be sampled (satisfied for CASES-97, but not for the IHOP_2002 eastern track, since stations 7–9 sample grassland only), and horizontal variability in H and LE must be greater than ~100 W m^{-2} (LeMone et al. 2003), based on the 50 W m^{-2} uncertainty in the measurements (Yates et al. 2001).

Because the IHOP_2002 surface sites sample grassland only, we turned to aircraft data to estimate Δ_{xy}LE/$\Delta_{xy}H$ for the days in Fig. 4. In addition to the above

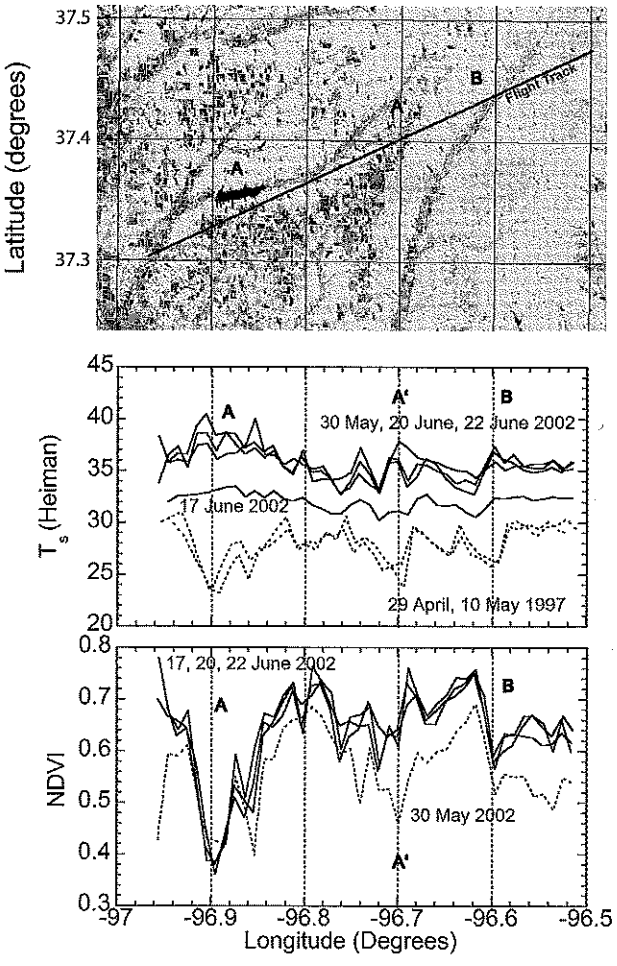

FIG. 7. (top) Flight track and 60-m-resolution land use based on National Land Cover Data (NLCD) 1992 data available online at http://landcover.usgs.gov. (middle) Radiometric surface temperature T_s for all six days. (bottom) NDVI for four IHOP_2002 days. Numbers are ~1 km averages, over all the legs flown on the day specified. Land-use shading: light gray: grasslands; medium gray: row crops; darker gray: small grains; black: open water. **A** and **A′** correspond to areas of winter wheat, and **B** to the easternmost riparian zone along the flight track.

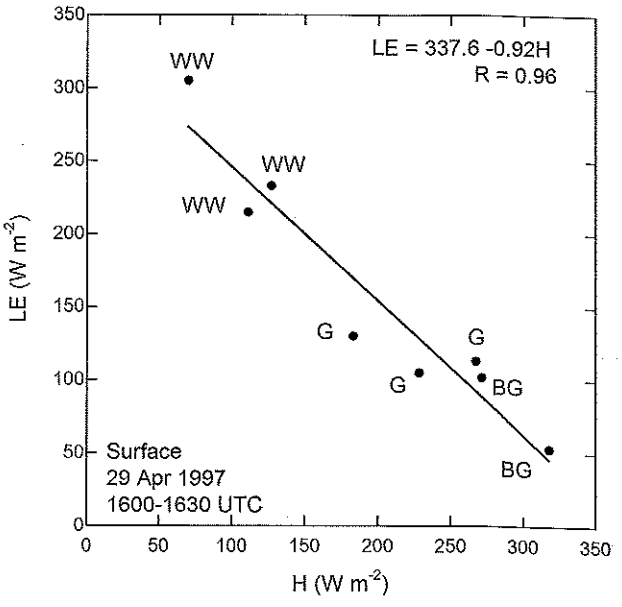

FIG. 8. LE as a function of H, for 1600–1630 UTC 29 April (CASES-97) from surface-station data, after more than a week of dry-down. Data from each site labeled according to ground cover: WW = winter wheat, G = grass, BG = bare ground.

requirements, slope estimates from aircraft data need a sufficient sample to overcome the positive $\Delta_{xy}\mathrm{LE}/\Delta_{xy}H$ slope that results from the atmosphere's tendency to concentrate fluxes in the upwelling regions of large eddies (e.g., LeMone 1976; Grossman 1982). This often necessitates horizontal as well as temporal averaging (LeMone et al. 2003). Figure 9 shows $\Delta_{xy}\mathrm{LE}/\Delta_{xy}H$ as a function of horizontal averaging for IHOP_2002 (see Fig. 9 in LeMone et al. 2003 for a similar plot for CASES-97). As in Fig. 8, the slopes are based on least squares linear regression. Aircraft–surface slope comparisons for three days along the western track, where four surface stations sampled the range of land cover, show the best match for 3–5-km aircraft averages, precisely the range at which we would expect effects of boundary layer large eddies to be mostly filtered out (~3 z_i; see Table 2; z_i values on the western track are similar for the days compared; Kang et al. 2007). Consistent with this, the slope in Fig. 9 tends to level off at averaging lengths >5 km. Thus we will use 3–5-km averages in slope comparisons, even though LeMone et al. (2003) suggested longer averages were needed to match surface slopes in CASES-97. Of course, a rigorous determination of the best average requires good aircraft statistics and corresponding surface data. The picture is complicated by potentially different footprints for H and LE (e.g., Kustas et al. 2006) and different atmospheric factors affecting H and LE at larger scales.

As in CASES-97, we could not determine reasonable $\Delta_{xy}\mathrm{LE}/\Delta_{xy}H$ slopes for all the days. The most robust slope estimates, both for aircraft and surface data, are for days with the longest dry-down and driest soils, 29 April 1997 and 22 June 2002. No amount of filtering is

TABLE 5. Selected correlations for IHOP_2002 4-km filtered grand-average legs.

Date	Legs	NDVI-T_s	H-T_s	LE-T_s	H-NDVI	LE-NDVI
30 May	8	−0.65	0.05	−0.10	−0.50	0.21
17 Jun	6	−0.72	0.57	−0.04	−0.68	0.14
20 Jun	5	−0.84	0.37	0.01	−0.50	−0.11
22 Jun	10	−0.86	0.73	−0.61	−0.77	0.54

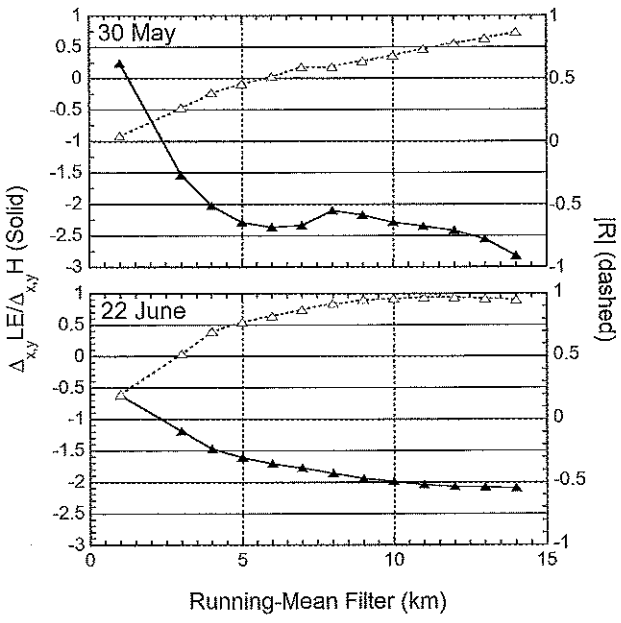

FIG. 9. For 30 May and 22 June, slope $\Delta_{xy}LE/\Delta_{xy}H$ and absolute value of the associated correlation coefficient R as a function of horizontal running-mean average.

sufficient to make the slopes negative on 17 or 20 June. On 17 June, the high soil moisture and cool, near-uniform T_s (Fig. 4) results from recent rainfall; thus we expect LE due to evaporation from bare or sparsely covered ground is comparable to LE due to evapotranspiration over green vegetation (e.g., Yates et al. 2001). In such cases, horizontal variability in H and LE should be comparable to horizontal variability in the available energy $R_{net} - G_{sfc}$, with an H versus LE plot a cloud of points without a well-defined slope. Further, the rainfall distribution could be important. On 20 June, horizontal variability in available energy is significantly altered by clouds (Fig. 3), and only five low-level legs were flown. With only four days to compare, we will look at more days from CASES-97 and use land surface models.

b. *Effect of the diurnal cycle on* $\Delta_{xy}LE/\Delta_{xy}H$

IHOP_2002 aircraft flux patterns were centered on local solar noon (~1800–1900 UTC; Table 1), while CASES-97 aircraft data used here were centered at ~1630 UTC. Figure 10 shows the change of $\Delta_{xy}LE/\Delta_{xy}H$ between 1515 and 2145 UTC, for an idealization of 22 June with two types of land cover, grass, and sparse vegetation. Over grasses, H peaks earlier than LE, and G_{sfc} is smaller in the afternoon than in the morning. If G_{sfc}, H, and LE over dormant vegetation are more symmetric about solar noon (true for CASES-97; see LeMone et al. 2000, 2002), the combined behavior of these two land-cover types makes the slope more negative with time (by ~0.1 h^{-1}). The IHOP_2002 aircraft slopes for 22 June show a similar trend: for the first five legs, the 4-km-average slope is −1.25 ($|R|$ = 0.4), shallower than the value for the second five legs, −1.5 ($|R|$=0.66), again a ~0.1 h^{-1} decrease. For CASES-97, half-hour-average plots of $\Delta_{xy}LE/\Delta_{xy}H$ from half-hour-averaged surface-station data centered from 1745 to 2115 UTC revealed no obvious trend for 10 May, but 29 April slopes became shallower with time (+0.05 h^{-1}).

c. *The association of shallower* $\Delta_{xy}LE/\Delta_{xy}H$ *slopes with longer dry-down and drier soils*

Figure 11 shows $\Delta_{xy}LE/\Delta_{xy}H$ as a function of time for the three observed CASES-97 dry-down periods described in Fig. 7 of Yates et al. (2001), and for the modeled IHOP_2002 17–22 June 2002 dry-down period. For three of the four dry-down periods, $\Delta_{xy}LE/\Delta_{xy}H$ becomes shallower with time after rainfall, with the final point of the 9–12 May CASES-97 sequence leading to the one exception. The IHOP_2002 slopes in the bottom frame are averages of the 4-km square model grids along the eastern track, from the High-Resolution Land Data Assimilation System (HRLDAS). HRLDAS, which is based on the Noah LSM, is described and evaluated in Chen et al. (2007). Diurnal effects are not a factor here, since the time of day is kept constant.

The relationship of $\Delta_{xy}LE/\Delta_{xy}H$ to soil moisture is illustrated for both field programs in Fig. 12. The LSM slopes in the bottom two frames come from a variety of LSMs. For CASES-97, the slopes come from Fig. 5 of LeMone et al. (2003), and are based on the following three LSMs: SOLVEG (Nagai 2002), the Noah model (OSULSM; Pan and Mahrt 1987; Chen et al. 1996; Ek et al. 2003), and the National Center for Atmospheric Research (NCAR) LSM (Bonan 1996). The LSM data used to compute CASES-97 slopes were derived for 1-km squares as described in Chen et al. (2003), and smoothed with a ~4 km running mean to be consistent with the corresponding aircraft fluxes. An additional version of the Noah model (Noah) for 1-km squares along the track is included because soil-moisture data from the other three are no longer available. Of the available CASES-97 model runs, it had the closest values to the modeled soil moisture in Chen et al. (2003). The CASES-97 LSMs are evaluated in Yates et al. (2003) and Chen et al. (2003).

The 5-cm volumetric soil-moisture values in Fig. 12 are computed to match the slope data to the degree possible. For the CASES-97 slopes based on the surface array (Fig. 2 of LeMone et al. 2003, sites 1–8), the cor-

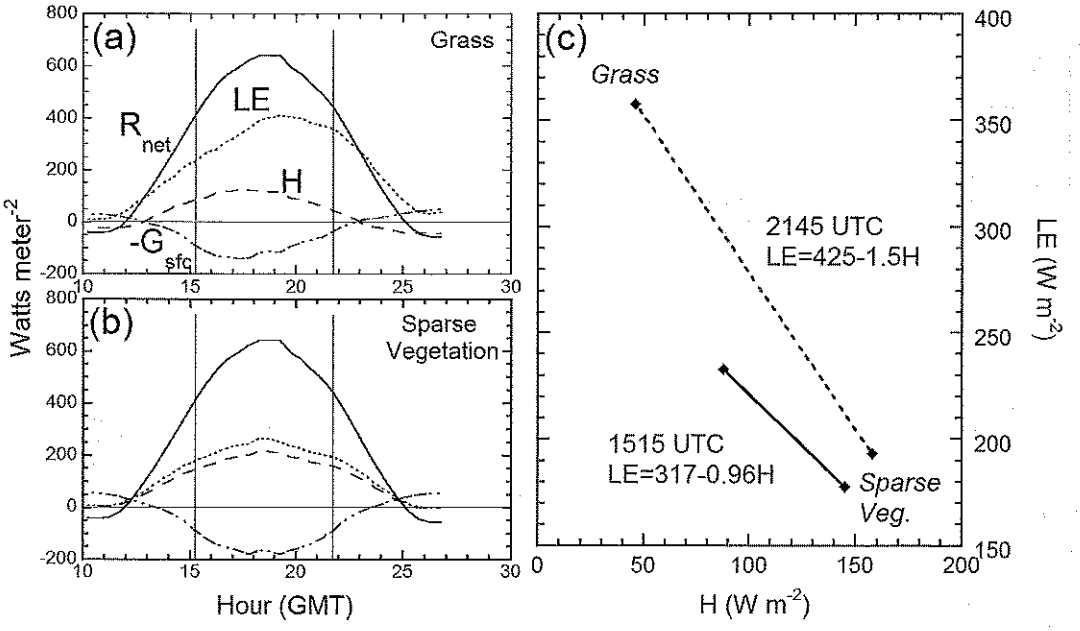

FIG. 10. Change in $\Delta_{xy}\mathrm{LE}/\Delta_{xy}H$ between 1515 and 2145 UTC, for idealized bimodal land-cover distribution (grass and sparse vegetation) using 22 June and CASES-97 data. Surface energy budgets with lines defined as in Fig. 3, for (a) grass, based on average for stations 7–9 but with cloud effect eliminated, and (b) sparse vegetation, assuming "cloudless" R_{net} but a "sparse mostly dormant vegetation" signature similar to that for CASES-97 (e.g., LeMone et al. 2000), with H, LE, and G_{sfc} symmetric about solar noon (1830 UTC); $H = 0.82$ LE and G_{sfc} on average 40% larger than that for grass. (c) $\Delta_{xy}\mathrm{LE}/\Delta_{xy}H$.

responding soil-moisture values were averaged. The National Oceanic and Atmospheric Administration (NOAA) Twin Otter–based slope in Fig. 12a also uses the CASES-97 array average soil moisture, since its flight track was farther north within the array (Fig. 2, track 3, of LeMone et al. 2003). For the slopes based on the King Air, averages of IHOP_2002 sites 7–9 are used for 30 May and 22 June 2002, while the volumetric soil moisture at CASES-97 site 6 (closest to the eastern track) is used for the 29 April aircraft slopes. Horizontal variation of the Noah model soil moisture along the eastern track suggests that site 6 values are similar to track averages. For the CASES-97 array-averaged soil moisture for all three days, the spatial standard deviation is large (~0.1), but the day-to-day trend is the same for all eight stations and consistent with the trend for the Noah LSM (Fig. 12b). For IHOP_2002, the range of soil-moisture values for sites 7–9 varies between 0.016 (17 June) and 0.057 (22 June), with the 30 May value = 0.027. HRLDAS soil-moisture values qualitatively follow the observed day-to-day trend.

Subject to the uncertainties discussed in the foregoing, all three frames of Fig. 12 suggest that $\Delta_{xy}\mathrm{LE}/\Delta_{xy}H$ becomes shallower with drier soils. The trend for the observations, in Fig. 12a is particularly striking, but must be interpreted with caution given the uncertainty in the slope and soil-moisture estimates. Correcting the slope data to a common time (1800 UTC) to allow for diurnal effects in Fig. 12a changes values from ~0.1 to 0.15—a negligible effect.

As in the case of the observed slopes, the LSM values for CASES-97 in Fig. 12b are more well defined for 29 April than for 10 or 20 May. For 10 and 20 May, there is usually smaller horizontal variability and more scatter around the best-fit lines used to determine the slope in Fig. 5 of LeMone et al. (2003). Slopes based on poor statistical fits are omitted; hence the figure shows fewer points for 10 May (3) and 20 May (4) than for 29 April (6). Indeed, the horizontal variability in H and LE was not sufficient to define a slope even with surface data on 20 May.

Given the uncertainty in soil-moisture values, point-by-point comparisons of $\Delta_{xy}\mathrm{LE}/\Delta_{xy}H$ show the average LSM values match the surface slopes reasonably well for 29 April and 10 May (CASES-97), but the modeled slopes for IHOP_2002 are much shallower than those observed. This is consistent with HRLDAS significantly underestimating the soil moisture in Fig. 12c. The discrepancy is at least in part due to using as input the NCEP stage-IV radar-derived rainfall, which is up to 1/3 less than that observed at sites 7–9 (Chen et al. 2007). For CASES-97, 1-km-resolution gauge-corrected rainfall data generated as part of the experiment were used as input for the CASES-97 LSMs (Yates et al.

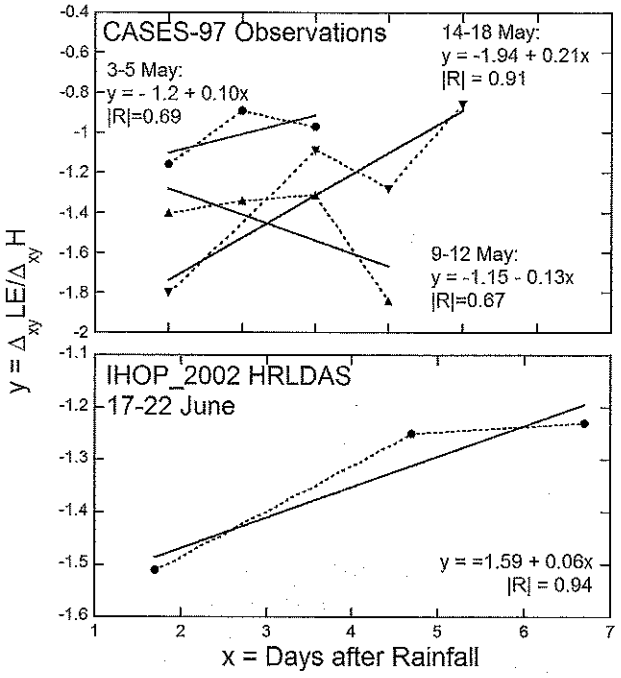

FIG. 11. Slope $\Delta_{xy}H/\Delta_{xy}$LE as a function of time after rainfall. (top) The three CASES-97 dry-down sequences of Yates et al. (2001). Slopes are calculated from fluxes at eight or nine stations, and averaged 4 h after eliminating sites/times with low R_{net} (clouds); average centered on 1830 UTC (~solar noon). Correlation coefficients for slopes in chronological order: 3–5 May, R = 0.93, 0.78. 0.87; 9–12 May: 0.87. 0.87, 0.83, 0.79; 14–18 May: 0.82, 0.87, 0.90, 0.81. (bottom) IHOP_2002 17–22 Jun 2002 dry-down, based on 4-km HRLDAS data averaged along eastern track, averaged 1600–1900 UTC.

2001; Chen et al. 2003), leading to values more consistent with observations.

Collected in a nearby and similar geographic area, the FIFE data in Table 6 suggest similar behavior: Δ_{xy}LE/$\Delta_{xy}H$ is steepest for the wettest phase and shallowest for the driest phase. If one accepts the total FIFE fluxes as reasonable proxies for the daytime flux and assumes that the rainfall was reasonably spaced through the field observations, these figures are consistent with steeper slopes with wetter soils and/or shorter time between rain events.

d. Idealized Noah model runs

To examine the source of the Δ_{xy}LE/$\Delta_{xy}H$ differences further, we apply the Noah model to two pairs of idealized scenarios (Table 7) to represent CASES-97 (spring) and IHOP_2002 (summer). In each case, only two types of land cover—crops (winter wheat) and grassland—are represented according to changes in their green vegetation fraction Fg. The assumed soil depth is 2 m, the assumed root depth is 1 m, and there

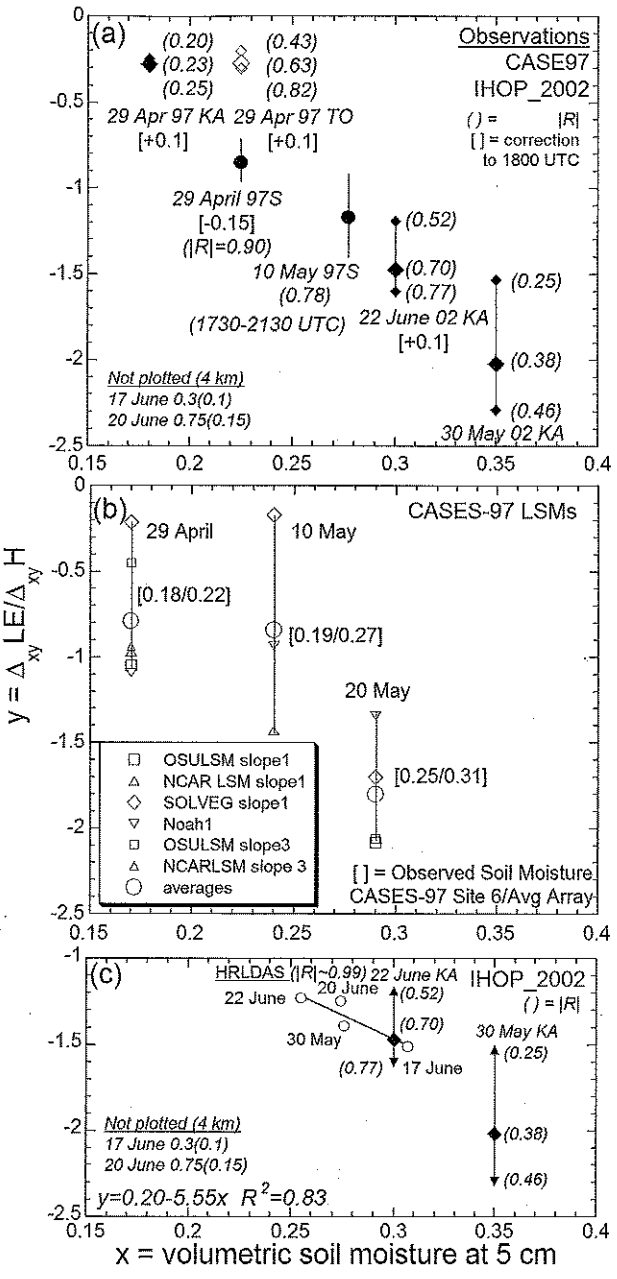

FIG. 12. Slope Δ_{xy}LE/$\Delta_{xy}H$ as a function of volumetric soil moisture at 5 cm, for (a) observations; (b) CASES-97 LSMs, based on scatterplots in Fig. 5 of LeMone et al. (2003); (c) IHOP_2002 HRLDAS LSM with aircraft-derived fluxes included. LSM slopes = open symbols. In key to (b), 1 = eastern track, and 3 = CASES-97 track 3. Observed slopes = filled-in symbols. For surface: circles; for aircraft: 3-km average = up triangles; 4-km average = diamonds; 5-km average = down triangles; King Air (KA) = black; NOAA Twin Otter (TO) = gray. Italic numbers in parentheses: correlation coefficient |R| for aircraft slope plots like Fig. 9; for surface, average of 0.5-h slope correlation coefficients for plots like Fig. 8. In (c), best-fit line is based on HRLDAS values. NOAA Twin Otter data are described in LeMone et al. (2003). For further details, see text.

TABLE 6. Slope $\Delta_{xy}LE/\Delta_{xy}H$ based on average flux data for FIFE, by phase, based on data in Table 6 of Fritschen and Qian (1992).

Date	Rainfall	Surface data slope ($\|R\|$) combined data
26 May–16 Oct 1987	Wettest	−2.48 (0.88)
10 May–18 Sep 1988	Intermediate	−1.36 (0.89)
21 Jul–13 Aug 1989	Driest	−1.09 (0.87)

is no horizontal transport of water. Soil layers were 95% saturated at the beginning of the experiments, and allowed to dry down for 15 days. Diurnal forcing (net solar radiation) was consistent with clear skies and is the same for all runs.

The $\Delta_{xy}LE/\Delta_{xy}H$ slopes for the four dry-down scenarios are represented by lines connecting noontime H and LE values for crops and grassland for each day in Fig. 13. In all cases, the steepest $\Delta_{xy}LE/\Delta_{xy}H$ slopes occur immediately following rainfall. The range of flux values on each day is larger than observed because of the extreme initial conditions. Subsequently, the line connecting the two vegetation types rotates counterclockwise with time from a steep slope (between –1.8 and –2.6) to a shallower value (between −1.4 and −1.9) on day 15, and the range of values increases, as in the observations. For the vegetation type with Fg = 0.95, H and LE remain nearly constant[2] until around day 15, while the end of the line with low Fg moves down and to the right with time at a roughly 45° angle, as LE decreases and H increases with time. In the scenarios with Fg = 0.50 for the greener vegetation, both ends of the line move down their respective ~45° time-evolution paths, but the Fg = 0.05 end moves slightly faster, again rotating the $\Delta_{xy}LE/\Delta_{xy}H$ line toward shallower slopes with time.

From (5), the separation between the two time-evolution paths in each frame of Fig. 13 is determined by the value of $R_{net} - G_{sfc} = H + LE$. At a given time, the difference in R_{net} for the two vegetation types is small (true for CASES-97; see Fig. 9 of LeMone et al. 2000), so this separation is primarily because the heat flux into the soil is significantly larger for the low-Fg vegetation than for the high-Fg vegetation, resulting in smaller $R_{net} - G_{sfc}$ for the lower-Fg vegetation. As long as this is true, the low-Fg time-evolution path (numbered symbols) will be closer to the origin (H + LE smaller) than the high-Fg time-evolution path (symbols at the other end of the $\Delta_{xy}LE/\Delta_{xy}H$ lines). Because drier soil has lower thermal conductivity, G_{sfc} decreases with time. However, $[\partial(R_{net} - G_{sfc})/\partial t] = [\partial(H + LE)/\partial t] \sim 0$ in the scenarios shown, since the warming surface temperature T_s increases upwelling infrared radiation ($\propto T_s^4$) just fast enough for R_{net} to decrease at nearly the same rate as G_{sfc}. This makes the time-evolution paths ($\Delta_t LE/\Delta_t H$) parallel with a ~45° slope. In some simulations (not shown), $|(\partial G_{sfc}/\partial t)| > |(\partial R_{net}/\partial t)|$ for the lower-Fg vegetation, making $[\partial(R_{net} - G_{sfc})/\partial t] = [\partial(H + LE)/\partial t] > 0$. This reduces the distance between the two time-evolution paths with time and allows $\Delta_{xy}LE/\Delta_{xy}H$ to reach or exceed −1.

TABLE 7. Vegetation characteristics for Noah LSM runs. Soil = silty clay loam.

Scenario	Quantity	Crop	Grass
Early spring (late April)	Greenness fraction (Fg)	0.50	0.05
Late spring (early–mid-May)	Greenness fraction (Fg)	0.95	0.50
Summer1 (no grazing—CRP* grass)	Greenness fraction (Fg)	0.05	0.95
Summer2 (pasture grass—grazed)	Greenness fraction (Fg)	0.05	0.50
All scenarios	Leaf area index	4.2	3.1
All scenarios	Root depth**	1 m	0.1–1.0 m

* CRP = U.S. Department of Agriculture Conservation Reserve Program (assumed ungrazed).
** All root depths 1 m for Fig. 13.

e. *The effect of terrain on $\Delta_{xy}LE/\Delta_{xy}H$ slopes*

Knowing the association of grassland, shallow soils, and bedrock exposures with ridges, and the association of crops and deeper soils with nearby valleys along the eastern track (LeMone et al. 2000), we can speculate on how terrain would affect the modeled slopes in Fig. 13. For CASES-97 (spring), the dormant grasses should dry down faster than in the figure, because (a) the shallower soils will dry out faster, (b) surface runoff will make less moisture available, and (c) subsurface water will flow downhill. This will accelerate the "grassland" end of the $\Delta_{xy}LE/\Delta_{xy}H$ line downward and to the right. We represent this dry-down "acceleration" by an arrow pointing down and to the right next to the grass time-evolution path (numbered symbols) in the top frames of the figure. Similarly, we use an arrow pointing upward and to the left to indicate some slowing of the dry-down for the crops (WW) due to water supply from

[2] Though the duration of near-constancy is extreme, the trends are qualitatively consistent with Fig. 7 in Yates et al. (2001) for three CASES-97 dry-downs: noontime values of LE changed little for 3–5 days for the green vegetation, and decreased rapidly over bare ground. For IHOP_2002, the LE diurnal pattern changed little during the late-June dry-down represented by 17, 20, and 22 June in Fig. 3.

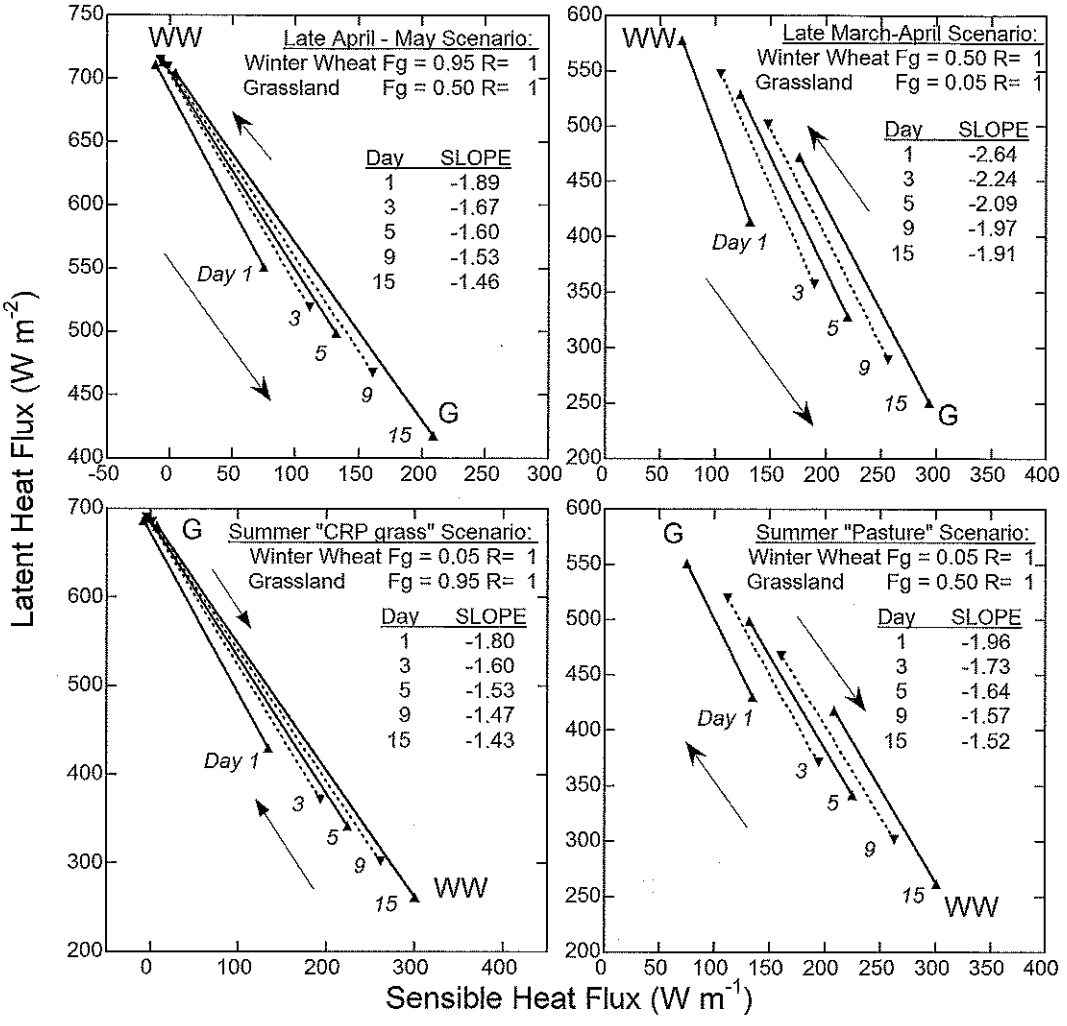

FIG. 13. Idealized horizontal variability of noontime H and LE, in terms of the slope $\Delta_{xy}\mathrm{LE}/\Delta_{xy}H$, for two "spring" (CASES-97) and two "summer" (IHOP_2002) dry-down scenarios, based on the Noah LSM with input described in Table 7. The slopes are represented by straight lines connecting the two major land-use types near the eastern track, winter wheat (WW), and grassland (G). The lines alternate between solid (with up-triangle end points) and dashed (with down-triangle end points); each set of end points defines the time-evolution path for a given land cover; the numbers adjacent to the time-evolution path for the lower-Fg ground cover correspond to the number of days of dry-down simulated; Fg = greenness fraction; R = root depth in m. For further description, see text.

surface runoff and subsurface flow. Together, these factors should produce an ~ -1 slope more rapidly than the simulations represented in the figure.

Conversely, accounting for terrain in the IHOP_2002 (summer) scenario, the dry-down should be accelerated for the green grasses (down-right-pointing arrow next to the grass time-evolution path in the lower frames, and slowed in the valleys, where there is dormant or harvested crop with low Fg (up-left-pointing arrow). This slows down the evolution of $\Delta_{xy}\mathrm{LE}/\Delta_{xy}H$ to shallower slopes.

Figure 14 shows the impact of decreasing the Noah LSM grass-rooting depth (a crude proxy for "soil depth") on $\Delta_{xy}\mathrm{LE}/\Delta_{xy}H$. Decreasing the root depth from 1 m (the value corresponding to Fig. 13) to 10 cm leads to shallower slopes for the spring scenario, and steepens the slopes for the summer scenario, as expected. However, these changes are small compared to those associated with the length of dry-down (or equivalently, the amount of soil moisture). The effect of relative surface elevation on dry-down near the eastern track is supported by Fig. 15 of Grossman et al. (2005), which shows that T_s increases with elevation *for a given land-use type* in CASES-97. Thin soil at higher elevations is mentioned as a major factor. D. Gochis (2005, personal communication) modified the Noah model to

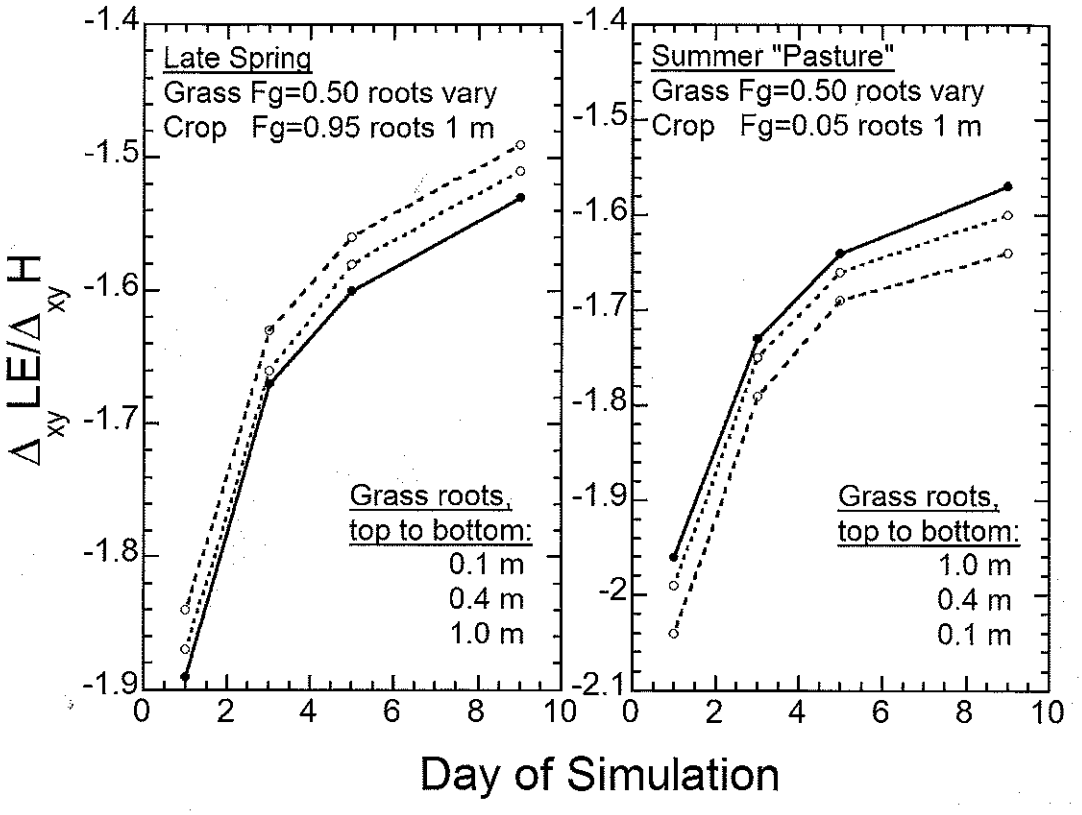

FIG. 14. Sensitivity of Noah model $\Delta_{xy}H/\Delta_{xy}$LE slopes to grass rooting depth, as a function of day of simulation (time after rainfall). Lines correspond to grass rooting depth: 1 m (solid line), 0.4 m (dotted line), and 0.1 m (dashed line). For model input parameters, see Table 7.

include horizontal transport of water ("routing") for a simulation of CASES-97 fluxes, and this resulted in slightly faster dry-downs on the ridges, with slightly higher H and lower LE with the routing included. This work is ongoing.

5. Discussion and conclusions

Analysis of aircraft, surface-flux tower, and radar wind profiler data on six fair-weather days with southerly winds and nearly clear skies from CASES-97 and IHOP_2002 shows that land-use patterns have strong influence on the horizontal distribution of sensible and latent heat fluxes H and LE over southeastern Kansas; combined with LSM runs, the data suggest that soil moisture influences the relative magnitude of H and LE horizontal variations. In both field programs, H maxima occur over dormant/sparse vegetation, with minima over green vegetation; to a lesser degree, LE maxima occur over green vegetation, with minima over dormant/sparse vegetation. Small day-to-day differences in flux distribution occur due to the effect of wind direction and speed and surface buoyancy fluxes on the scale of the surface heterogeneity felt (fetch) as well as statistical uncertainty. The soil moisture and length of time after rainfall affect the amplitude and coherence of the LE and H horizontal patterns. We suggest terrain could also modulate the horizontal variability in fluxes in this region. Fluxes are calculated from departures from flight-leg linear trends, but those estimated relative to 1-km means showed similar horizontal patterns, with 1-km departure fluxes showing the expected smaller averages, horizontal variability, and standard deviations.

Combining the data from CASES-97 (spring) and IHOP_2002 (summer) allows a clear picture of the effects of land-use distribution on the horizontal distribution of H and LE along the eastern track, because the dominant vegetation types—grassland and winter wheat—reverse roles. During CASES-97, the winter wheat grew rapidly, and the grass was dormant (29 April) and then greening up (10 May), while during IHOP_2002 the grass was green and the winter wheat was senescent (for 30 May) or harvested (17, 20, 22 June). Thus, H maxima for IHOP_2002 and H minima for CASES-97 reflect winter wheat beneath and to the south of the track, while H minima for IHOP_2002 and H maxima for CASES-97 reflect grassland beneath and

to the south of the track. For LE there is a weaker tendency for higher values over the green vegetation and lower values over the dormant vegetation. Consistent with this, high H values correspond to high T_s and low values of NDVI, while, to a lesser degree, high values of LE correspond to high NDVI and low T_s for both field programs.

For days with few or no clouds, using observations and LSMs to quantify H and LE horizontal variability in terms of the slope $\Delta_{xy}\mathrm{LE}/\Delta_{xy}H$ for plots of LE as a function of H at a given time suggests the following time sequence: right after rainfall, H and LE are relatively uniform with no well-defined slope, after which a slope emerges (~ -2), which gets shallower (~ -1) and better defined with time during soil dry-down. Consistent with this behavior, moister soil tends to be associated with steeper slopes. Rainfall is ample, so the vegetation never becomes stressed. Noah model runs for idealized CASES-97 and IHOP_2002 scenarios suggest that flux into the soil has an important role in determining the slope by reducing the available energy $R_{\mathrm{net}} - G_{\mathrm{sfc}}$ for the less-green or dormant vegetation. Because H, LE, and G_{sfc} can peak at different times at some locations, the slope can also vary as a function of time of day, but this effect is small since slopes were computed for similar times.

Other things being equal, the idealized Noah runs also suggest that the relationship of vegetation with terrain could lead to steeper slopes for IHOP_2002 (June–July) than for CASES-97 (April–mid-May), but the effect is small. The association of grass with ridges (due to shallow soil and bedrock exposures) and winter wheat with valleys (deep enough soil to cultivate) should affect the rate of dry-down and the associated evolution of H and LE. In the spring, the dormant grass on the ridges should dry down faster than for no terrain, because of shallower soil and surface and subsurface runoff (less water available), while the dry-down of the green winter wheat should be slowed by water supplied from higher elevations. This should accelerate the trend of the slopes to shallower values for CASES-97. Conversely, in IHOP_2002, the accelerated dry-down of the green grasses and slowed dry-down of the dormant or harvested winter wheat should slow the tendency of the slope to become shallower with time.

The relationship of $\Delta_{xy}H/\Delta_{xy}\mathrm{LE}$ to length of dry-down and soil moisture are suggestive, but more data are needed to obtain definitive results, and the analysis is limited to one geographic area. IHOP_2002 slopes are based on aircraft data, and CASES-97 slopes primarily on surface data, and there are only a few cases to draw from. There are no IHOP_2002 surface-station-based slopes along the eastern track for deciding what filter length is best to calculate aircraft-derived slopes, so we chose 4 km based on western-track aircraft and surface data. Four LSMs suggest an association of steeper slopes with moister soils, and one (HRLDAS) was used to document shallower slopes with time after rainfall; it would be desirable to use the same LSM(s) for the whole dataset. Looking at soil moisture through the root zone would be of interest, but such data are not available for CASES-97. Idealized LSM runs and the results of Grossman et al. (2005) suggest terrain effects could lead to steeper slopes for IHOP_2002, but definitive observational evidence is lacking.

While several investigators have used aircraft data to evaluate surface fluxes (e.g., Schuepp et al. 1992; Mahrt 2000; Song and Wesely 2003; Isaac et al. 2004; Kustas et al. 2006), statistical uncertainties continue to plague such comparisons. Many investigators have used high-pass filtering to reduce the uncertainty, and LeMone et al. (2003) suggest horizontally averaging the aircraft data to remove the effects of concentration of fluxes by large eddies and to increase statistical robustness, and then applying an equivalent filter to the LSM data to make the two datasets comparable. However, the possibility that source regions for H and LE might not be equivalent (Kustas et al. 2006), and the possibility that atmospheric processes could affect H and LE differently at larger scales, leads to questions of how filtering affects the effective sources and hence $\Delta_{xy}\mathrm{LE}/\Delta_{xy}H$. Spring and summer data are needed from an array of surface-flux stations over representative land-use types, and repeated aircraft flux measurements are needed to quantify seasonal surface heterogeneity effects and determine the best way to filter aircraft data.

Future plans include comparisons of the estimated fluxes with surface-flux and soil-moisture maps generated using the Noah model, initialized with HRLDAS (Chen et al. 2007), and comparisons with satellite products, building on the results of Chen et al. (2003). Both comparisons will enable a more quantitative assessment of the effects of the upstream flux footprint, following Schuepp et al. (1992), Song and Wesely (2003), and others. In addition, we wish to explore the evolution of $\Delta_{xy}\mathrm{LE}/\Delta_{xy}H$ in the Noah model and other LSMs, and look at other datasets to see if similar patterns emerge.

Acknowledgments. This work would not have been possible without the commitment, enthusiasm, and expertise of the Wyoming King Air aircrew, the staff maintaining the Wyoming Cloud Radar, National Center for Atmospheric Research staff maintaining the surface-flux instruments, and the students taking the manual observations at the flux sites. The NCAR portion of this research was supported by USWRP Grant

NSF 01 and the NCAR Water Cycle Initiative. RLG's participation in IHOP_2002 was supported by NSF Grant ATM-0296159. RC's work was supported by the U.S. Department of Energy, Office of Biological and Environmental Research, under Contract W-31-109-Eng-38. We also thank Ken Davis, Ronald Dobosy, Peter Isaac, and a fourth anonymous reviewer for contributing significantly to tightening the final manuscript, and John Finnigan for useful discussions.

REFERENCES

Anthes, R. A., 1984: Enhancement in convective precipitation by mesoscale variations in vegetative covering in semiarid regions. *J. Climate Appl. Meteor.,* **23,** 541–554.

Bonan, G. B., 1996: A land surface model (LSM version 1.0) for ecological, hydrological, and atmospheric studies: Technical description and users guide. NCAR Tech. Note NCAR/TN-417+STR, 150 pp. [Available from NCAR Library, P.O. Box 3000, Boulder, CO 80307.]

Chen, F., and Coauthors, 1996: Modeling of land-surface evaporation by four schemes and comparison with FIFE observations. *J. Geophys. Res.,* **101,** 7251–7268.

——, R. Pielke Sr., and K. Mitchell, 2001: Development and application of land-surface models for mesoscale atmospheric models: Problems and promises. *Observation and Modeling of Land Surface Hydrolological Processes,* V. Lakshmi, J. Alberston, and J. Schaake, Eds., Amer. Geophys. Union, 107–135.

——, D. N. Yates, H. Nagai, M. LeMone, K. Ikeda, and R. Grossman, 2003: Land surface heterogeneity in the Cooperative Atmosphere Surface Exchange Study (CASES-97). Part I: Comparing modeled surface flux maps with surface-flux tower and aircraft measurements. *J. Hydrometeor.,* **4,** 196–218.

——, and Coauthors, 2007: Description and evaluation of the characteristics of the NCAR High-Resolution Land Data Assimilation System. *J. Appl. Meteor. Climatol.,* in press.

Coulter, R. L., and D. Holdridge, 1998: A procedure for the automatic estimation of mixed layer height. *Proc. Eighth Atmospheric Radiation Measurement (ARM) Program Science Team Meeting,* Tucson, AZ, Department of Energy Office of Energy Research, 177–180.

Ek, M. B., K. E. Mitchell, Y. Lin, E. Rogers, P. Grummann, V. Koren, G. Gayno, and J. D. Tarplay, 2003: Implementation of the Noah land-use model advances in the NCAP operational mesoscale Eta Model. *J. Geophys. Res.,* **108,** 8851, doi:10.1029/2002JD003296.

Friehe, C. A., and D. Khelif, 1992: Fast response aircraft temperature sensors. *J. Atmos. Oceanic Technol.,* **9,** 784–795.

Fritschen, L., and P. Qian, 1992: Variation in energy balance components from six sites in the native prairie for three years. *J. Geophys. Res.,* **97** (D17), 18 651–18 661.

Geerts, B., and Q. Miao, 2005: The use of millimeter Doppler radar echoes to estimate vertical air velocities in the fair-weather convective boundary layer. *J. Atmos. Oceanic Technol.,* **22,** 225–246.

Grossman, R. L., 1982: An analysis of vertical velocity spectra obtained in the BOMEX fair-weather trade-wind boundary layer. *Bound.-Layer Meteor.,* **23,** 323–357.

——, 1992: Sampling errors in the vertical fluxes of potential temperature and moisture measured by aircraft during FIFE. *J. Geophys. Res.,* **97** (D7), 18 439–18 443.

——, D. Yates, M. A. LeMone, M. L. Wesely, and J. Song, 2005: Observed effects of horizontal radiative surface temperature variations in the atmosphere over a Midwest watershed during CASES 97. *J. Geophys. Res.,* **110,** D06117, doi:10.1029/2004JD004542.

Isaac, P. R., J. McAneney, R. Leuning, and J. M. Hacker, 2004: Comparison of aircraft and ground-based flux measurements during OASIS95. *Bound.-Layer Meteor.,* **110,** 39–67.

Kang, S., K. Davis, and M.A. LeMone, 2007: Observations of the ABL structures over a heterogeneous surface during IHOP_2002. *J. Hydrometeor.,* in press.

Kelly, R. D., E. A. Smith, and J. I. MacPherson, 1992: Comparison of surface sensible and latent heat fluxes from aircraft and surface measurements in FIFE 1987. *J. Geophys. Res.,* **97** (D17), 18 445–18 453.

Kustas, W. P., M. C. Anderson, A. M. French, and D. Vickers, 2006: Using a remote sensing field experiment to investigate flux-footprint relations and flux sampling distributions for tower and aircraft-based observations. *Adv. Water Resour.,* **29,** 355–368.

LeMone, M. A., 1976: Modulation of turbulence energy by longitudinal rolls in an unstable boundary layer. *J. Atmos. Sci.,* **33,** 1308–1320.

——, and Coauthors, 2000: Land–atmosphere interaction research and opportunities in the Walnut River watershed in southeast Kansas: CASES and ABLE. *Bull. Amer. Meteor. Soc.,* **81,** 757–779.

——, and Coauthors, 2002: CASES-97: Late-morning warming and moistening of the convective boundary layer over the Walnut River watershed. *Bound.-Layer Meteor.,* **104,** 1–52.

——, R. L. Grossman, F. Chen, K. Ikeda, and D. Yates, 2003: Choosing the averaging interval for comparison of observed and modeled fluxes along aircraft transects of a heterogeneous surface. *J. Hydrometeor.,* **4,** 179–195.

Lenschow, D. H., 1995: Micrometeorological techniques for measuring biosphere-atmosphere trace-gas exchange. *Biogenic Trace Gases: Measuring Emissions from Soil and Water,* P. Matson and R. Harriss, Eds., Blackwell Science, 126–163.

——, J. Mann, and L. Kristensen, 1994: How long is long enough when measuring fluxes and other turbulence statistics? *J. Oceanic Atmos. Technol.,* **11,** 661–673.

Mahrt, L., 2000: Surface heterogeneity and vertical structure of the boundary layer. *Bound.-Layer Meteor.,* **96,** 33–62.

Mann, J., and D. H. Lenschow, 1994: Errors in airborne flux measurements. *J. Geophys. Res.,* **99,** 14 519–14 526.

Miao, Q., B. Geerts, and M. A. LeMone, 2006: Vertical velocity and buoyancy characteristics of coherent echo plumes in the convective boundary layer, detected by a profiling airborne radar. *J. Appl. Meteor. Climatol.,* **45,** 838–855.

Nagai, H., 2002: Validation and sensitivity analysis of a new atmosphere–soil–vegetation model. *J. Appl. Meteor.,* **41,** 160–176.

Pan, H.-L., and L. Mahrt, 1987: Interaction between soil hydrology and boundary-layer development. *Bound.-Layer Meteor.,* **38,** 185–202.

Pazmany, A., R. McIntosh, R. Kelly, and G. Vali, 1994: An airborne 94 GHz dual-polarized radar for cloud studies. *IEEE Trans. Geosci. Remote Sens.,* **32,** 731–739.

Pielke, R. A., G. Dalu, J. Snook, T. Lee, and T. Kittell, 1991: Nonlinear influence of mesoscale land use on weather and climate. *J. Climate,* **4,** 1053–1069.

Raupach, R. R., and J. J. Finnigan, 1995: Scale issues in boundary-layer meteorology: Surface energy balances in heterogeneous terrain. *Hydrol. Processes,* **9,** 589–612.

Schotanus, P., F. T. M. Niewstadt, and H. A. R. DeBruin, 1983: Temperature measurements with a sonic anemometer and its application to heat and moisture fluctuations. *Bound.-Layer Meteor.,* **26,** 81–93.

Schuepp, P. H., J. I. MacPherson, and R. L. Desjardins, 1992: Adjustment of footprint corrections for airborne flux mapping over the FIFE site. *J. Geophys. Res.,* **97,** 18 455–18 466.

Segal, M., R. Avissar, M. McCumber, and R. Pielke, 1988: Evaluation of vegetation effects on the generation and modification of mesoscale circulations. *J. Atmos. Sci.,* **45,** 2268–2292.

Song, J., and M. L. Wesely, 2003: On comparison of modeled surface flux variations to aircraft observations. *Agric. For. Meteor.,* **117,** 159–171.

Trier, S. B., F. Chen, and K. W. Manning, 2004: A study of convection initiation in a mesoscale model using high-resolution land-surface initiation conditions. *Mon. Wea. Rev.,* **132,** 2954–2976.

Weckwerth, T., and Coauthors, 2004: An overview of the International H_2O Project (IHOP_2002) and some preliminary highlights. *Bull. Amer. Meteor. Soc.,* **85,** 253–277.

Yates, D. N., F. Chen, M. LeMone, R. Qualls, S. Oncley, R. Grossman, and E. Brandes, 2001: A Cooperative Atmosphere–Surface Exchange Study (CASES) dataset for analyzing and parameterizing the effects of land surface heterogeneity on area-averaged surface heat fluxes. *J. Appl. Meteor.,* **40,** 921–937.

——, ——, and H. Nagai, 2003: Land-surface heterogeneity in the Cooperative Atmosphere Surface Exchange Study (CASES-97). Part II: Analysis of spatial heterogeneity and its scaling. *J. Hydrometeor.,* **4,** 219–234.